Numerical Simulation of Vorticity Production in Shock Diffraction

T.-I. Tseng* and R.-J. Yang†

National Cheng Kung University, Tainan 701, Taiwan, Republic of China

Space–time conservation element and solution element method is employed with Euler and laminar Navier–Stokes solvers to investigate the vorticity production in shock diffraction and the interaction of the reflected shock wave with the main vortex for incident shock waves of various strengths diffracting around convex corners of different angles. The numerical results show that, in the Euler simulation, the flow structures are self-similar before they impinge on the bottom wall and that, in the laminar Navier–Stokes simulation, the flow structures are self-similar other than when they are influenced by the boundary-layer effect. Neither solver yields evidence of the rollup of small vortices along the slipstream. The major vorticity production is formed to be along the slipstream with the Euler solution. Different circulation production rates are observed between the Euler and Navier–Stokes solutions as a result of the vorticity contribution of the boundary layer and the secondary vortex in the latter. The degree of vorticity production is found to be dependent on the strength of the incident shock wave and the diffracting angle when the bottom wall effect is not considered.

Nomenclature

C_p	=	specific heat at constant pressure
C_v	=	specific heat at constant volume
e	=	total energy
F_{im}	=	inviscid flux vector of x component
F_{vm}	=	viscous flux vector of x component
G_{im}	=	inviscid flux vector of y component
G_{vm}	=	viscous flux vector of y component
k	=	thermal conductivity
M_s	=	incident Mach number
Pr	=	Prandtl number
p	=	pressure
q	=	heat conduction term
R	=	gas constant
Re	=	Reynolds number
T	=	temperature
T_0	=	temperature in front of incident shock
T^*	=	dimensionless time
t	=	time
U_m	=	flow variable vector
u, v	=	velocity components
V	=	velocity vector
V_s	=	speed of incident shock
x, y	=	Cartesian components
γ	=	ratio of specific heats
ε	=	internal energy
θ_d	=	diffracting angle
μ	=	dynamic viscosity
ρ	=	density
τ	=	shear stress term
ω	=	vorticity

I. Introduction

SHOCK wave diffraction around a convex corner is a fundamental problem in gasdynamics and is characterized by a complicated unsteady flow structure comprising a slipstream, a main vortex, a vortex shock, and a contact surface. In a strong incident shock, it has been observed that the flow structure also contains a terminator and a secondary shock. If viscous effects are ignored, the resulting flow development over time is found to be self-similar, that is, the flow pattern becomes frozen in the nondimensional coordinate system. (The coordinate system is non-dimensionalized by the speed of sound multiplying time.) Investigating the flow structures associated with shock diffraction is beneficial in developing a physical understanding of vortex production and the influence of the vortex strength on the flow structure.

The published literature contains many studies relating to the basic flow structures induced by shock wave diffraction around a convex corner. Howard and Mathews[1] investigated the shock diffraction problem and reported that the flow features included expansion waves, a slipstream, a contact surface, and vortices. Skews[2] performed a series of experimental studies into the shape of the shock wave diffracting around convex corners with diffracting angles ranging from 15 to 165 deg at incident Mach numbers between 1.0 and 4.0. The results indicated that the diffracted shock did not degenerate into a sound wave, even at large diffracting angles or low Mach numbers. In a second experimental study, Skews[3] reported that the flow structures were independent of the diffracting angle for angles greater than 75 deg in shock diffraction at incident Mach numbers ranging from 1.0 to 5.0. Dosanjh and Weeks[4] observed the mechanism of the interaction between a plane shock and a vortex and recorded the flow structure and the pressure distribution. Schardin[5] investigated the reflected shock and vortex interaction when a shock wave passed the wedge. Evans and Bloor[6] applied the vortex discretization method to study the process of vortex generation at a knife edge in a duct following weak shock diffraction. Bazhennova et al.[7] provided an explanation of the shock wave diffraction around an expansion corner in the unsteady interactions of shock wave propagation. However, no quantitative vortex strength was report in the cited works.

Shock wave diffraction has been the subject of many simulations concerning unsteady compressible flows. Takayama and Inoue[8] employed experimental and numerical methods to perform the benchmark testing of shock wave diffraction around a 90-deg convex corner with Mach numbers of 1.5. Hillier[9] used the explicit second-order Godunov-type Euler scheme to study the vortex generation caused by shock wave diffraction at a 90-deg convex edge.

Meanwhile, Sun and Takayama[10] studied the formation of a secondary shock wave behind a shock wave diffracting around a convex corner. Their results indicated that the secondary shock wave was formed as a result of the subsonic flow being accelerated to a locally supersonic condition. In a more recent study, Sun and Takayama[11] performed simulations using Euler and Navier–Stokes solvers to examine the secondary vortex generated in shock diffraction. Both solvers identified the formation of small vortices along the slipstream. However, these small vortices have never been observed in shock tube experiments. Kleine et al.[12] presented an overview of the flow features associated with a shock wave diffracted around a 90-deg corner and noted that subsonic and supersonic flows coexisted in the transition region.

Although the studies presented provided qualitative descriptions of the flow structures formed in shock diffraction, and discussed the generation of the vortices, the researchers did not attempt to quantify the vorticity production. Consequently, Sun and Takayama[13] used an Euler solver to quantify the vorticity production in shock wave diffraction around a sharp convex corner. Their results indicated that, if the effects of viscosity and heat conductivity are neglected, the vorticity production is dependent on the incident shock strength and the diffracting angle. Furthermore, the results showed that the slipstream is a more important source of vorticity than baroclinic effects.

Other than the study of Sun and Takayama,[13] few attempts have been made to quantify the strength of the vortices produced in shock wave diffraction around a convex corner. Moreover, Sun and Takayama employed only a Euler simulation in their study and chose not to investigate the reflected shock/vortex interaction. Accordingly, the present study employs both the Euler and the laminar Navier–Stokes solvers to quantify the vorticity production in shock wave diffraction and investigate the reflected shock/vortex interaction. Furthermore, in the present investigation, parametric studies are performed to determine the influence of the incident shock strength and the diffracting angle on the rate of vorticity production.

II. Numerical Method

Although the velocity distribution in high-speed flows can be measured experimentally, the resolution and accuracy of the obtained results are insufficient to permit quantification of the vorticity production in shock diffraction flows. Therefore, the present study investigates the vorticity production using numerical methods and assesses the vortex strength by considering the rate of circulation production.

A. Mathematical Model

The nondimensional equations of two-dimensional unsteady compressible Navier–Stokes flow can be written in Cartesian coordinates as

$$\frac{\partial U_m}{\partial t} + \frac{\partial (F_{im} - F_{vm})}{\partial x} + \frac{\partial (G_{im} - G_{vm})}{\partial y} = 0, \qquad m = 1, 2, 3, 4 \tag{1}$$

where $m = 1, 2, 3, 4$ indicates the continuity equation, the two momentum equations, and the energy equation, respectively. Furthermore, the flow variable vector U_m, the inviscid flux vectors F_{im} and G_{im}, and the viscous flux vectors F_{vm} and G_{vm} are given by

$$U = \begin{bmatrix} \rho \\ \rho u \\ \rho v \\ \rho e \end{bmatrix}, \quad F_i = \begin{bmatrix} \rho u \\ \rho u^2 + p \\ \rho u v \\ (\rho e + p)u \end{bmatrix}, \quad G_i = \begin{bmatrix} \rho v \\ \rho u v \\ \rho v^2 + p \\ (\rho e + p)v \end{bmatrix}$$

$$F_v = \begin{bmatrix} 0 \\ \tau_{xx} \\ \tau_{xy} \\ u\tau_{xx} + v\tau_{xy} - q_x \end{bmatrix}, \quad G_v = \begin{bmatrix} 0 \\ \tau_{yx} \\ \tau_{yy} \\ u\tau_{yx} + v\tau_{yy} - q_y \end{bmatrix}$$

where u and v, are x-component velocity and y-component velocity, respectively. Note that $e = \varepsilon + \frac{1}{2}(u^2 + v^2)$, where $\varepsilon = C_v T$ is the internal energy. When the ideal gas equation is used, $p = \rho R T$, then $p = (\gamma - 1)\rho\varepsilon$. The shear stresses and heat conduction terms are given by

$$\tau_{xx} = \frac{2}{3Re}\left(2\frac{\partial u}{\partial x} - \frac{\partial v}{\partial y}\right), \qquad \tau_{yy} = \frac{2}{3Re}\left(2\frac{\partial v}{\partial y} - \frac{\partial u}{\partial x}\right)$$

$$\tau_{xy} = \tau_{yx} = \frac{1}{Re}\left(\frac{\partial v}{\partial x} + \frac{\partial u}{\partial y}\right)$$

$$q_x = \frac{1}{(\gamma - 1)M_s^2 Re Pr}\frac{\partial T}{\partial x}, \qquad q_y = \frac{1}{(\gamma - 1)M_s^2 Re Pr}\frac{\partial T}{\partial y}$$

where $Re = \rho_0 V_S L/\mu_0$, $M_s = V_S/\sqrt{(\gamma R T_0)}$, and $Pr = C_P \mu_0/k_0$.

B. Conservation Element and Solution Element Method

The conservation element and solution element (CE/SE) method is distinguished by the simplicity of its conceptual basis, that is, flux conservation in space and time. Let $x_1 = x$, $x_2 = y$, and $x_3 = t$ be the coordinates of a three-dimensional Euclidean space E_3. The integral counterpart of Eq. (1) is

$$\oint_{S(V)} \mathbf{H}_m \cdot \mathrm{d}s = 0, \qquad m = 1, 2, 3, 4 \tag{2}$$

where $\mathbf{H}_m = (F_{im} - F_{vm}, G_{im} - G_{vm}, U_m)$ are the space–time current density vectors of the mass, x momentum, y momentum, and energy, respectively, and $S(V)$ is the boundary surface of an arbitrary space–time region V in E_3.

A quadrilateral spatial mesh is used to perform space–time integration, and the grid points are located at the centers of the quadrilaterals, in two spatial dimensions. At each grid point, four conservation elements (CEs) and a solution element (SE) are defined in connection with its four neighbors. For example, at point Q in Fig. 1a, the four CEs$^{(1)}$, $l = 1, 2, 3, 4$, are given by the quadrilateral cylinders $A_1B_1QB_4$ $A_1'B_1'Q'B_4'$(CE$^{(1)}$), $A_2B_2QB_1$ $A_2'B_2'Q'B_1'$(CE$^{(2)}$), $A_3B_3QB_2$ $A_3'B_3'Q'B_2'$(CE$^{(3)}$), and $A_4B_4QB_3$ $A_4'B_4'Q'B_3'$(CE$^{(4)}$), and the SE is defined by the union of the five planes $A_1B_1A_2B_2A_3B_3A_4B_4$, $B_1'B_1''Q'Q''$, $B_2'B_2''Q'Q''$, $B_3'B_3''Q'Q''$, and $B_4'B_4''Q'Q''$ with their immediate neighbors.

For any point (x, y) in SE(j, n), the flow variables are assumed to be continuous and $U_m(x, y, t)$, $F_{im}(x, y, t)$, and $G_{im}(x, y, t)$ are approximated by the first-order Taylor expansion as

$$U_m^*(x, y, t; j, n) = (U_m)_j^n + (U_{mx})_j^n(x - x_j)$$
$$+ (U_{my})_j^n(y - y_j) + (U_{mt})_j^n(t - t^n) \tag{3a}$$

$$F_{im}^*(x, y, t; j, n) = (F_{im})_j^n + (F_{imx})_j^n(x - x_j)$$
$$+ (F_{imy})_j^n(y - y_j) + (F_{imt})_j^n(t - t^n) \tag{3b}$$

$$G_{im}^*(x, y, t; j, n) = (G_{im})_j^n + (G_{imx})_j^n(x - x_j)$$
$$+ (G_{imy})_j^n(y - y_j) + (G_{imt})_j^n(t - t^n) \tag{3c}$$

where j and n indicate the jth element and the nth time step, respectively. Accordingly,

$$\mathbf{H}_m^*(x, y, t; j, n) = \left[F_{im}^*(x, y, t; j, n) - F_{vm}, G_{im}^*(x, y, t; j, n) \right.$$
$$\left. - G_{vm}, U_m^*(x, y, t; j, n) \right] \tag{4}$$

Hence, Eq. (2) can be approximated by its discrete counterpart, that is,

$$\oint_{CE(j,n)} \mathbf{H}_m^* \cdot \mathrm{d}s = 0, \qquad m = 1, 2, 3, 4 \tag{5}$$

The independent discrete variables of neighboring SEs are related through a local space–time flux conservation, which is enforced by
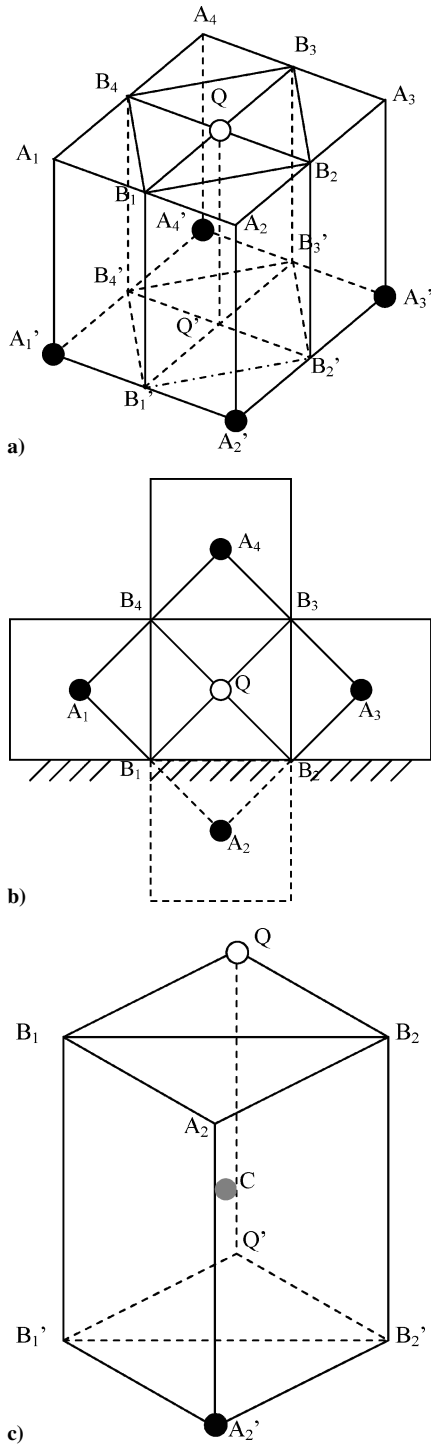
Fig. 1 Schematic of CE/SE scheme: a) definitions of CEs and SEs, b) mesh in two spatial dimensions, and c) CEs near wall boundary.

integrating Eq. (5) over a CE. Within a CE, contact discontinuities of the flow variables are permitted. Because space–time flux conservation is fundamentally correct both locally and globally, various CEs could be used to enforce the space–time integration given in Eq. (5). Integration over the CE provides a single discrete equation, which can be used to calculate $(U_m)_{i,j}^n$ at the new time level. If a contact discontinuity appears in the flow solution, the calculation of the spatial gradient, that is, $(u_{mx})_{i,j}^n$ and $(u_{mx})_{i,j}^n$, is further modified by a reweighting function to filter out the spurious oscillations caused by the jump. This procedure is referred to as the a–α scheme, where α is the weighting parameter. The details of this scheme have been presented by Chang,[14] Chang et al.[15] and Zhang et al.[16,17]

C. Boundary Treatment

The boundary treatments of the inlet boundary, symmetry boundary, complete reflection boundary, and non-reflection boundary are relatively straightforward in the CE/SE method. In traditional methods, different treatments are employed for the slip condition along the walls in inviscid flows and the nonslip condition in viscous flows. However, from a physical perspective, inviscid flow is simply an approximation that is adopted to simplify the calculation when viscous effects are unimportant. In the context of the CE/SE method, a novel and unified wall boundary treatment has been proposed for solving the Navier–Stokes equations. A schematic of the grid points near the horizontal wall is shown in Fig. 1b. It can be seen that no grid points are located on the wall, and hence, a ghost point, A_2, which is a mirror image of point Q with respect to the wall, is used. The flow variables and their spatial derivatives at the ghost point are obtained from point Q by the mirror image at each time level. Note that, in a traditional approach, the mirror image conditions are applied only to inviscid flows, that is, not to viscous flows. However, in the CE/SE method, the mirror image conditions are applied to both inviscid and viscous flows as will be explained.

The present calculations assume that the viscosity can be regarded as constant because the velocity is zero at the wall and the numerical solution is linear both in space and time within a solution element. It can be shown that the mass, x momentum, y momentum, and energy fluxes entering the cylinder $QB_1B_2\,Q'B_1'B_2'$ from the wall form the following row matrix:

$$
g_{w+} = S\left(0, \frac{-1}{Re}\frac{\partial u}{\partial y}, p - \frac{4}{3Re}\frac{\partial v}{\partial y}, \frac{-1}{Re\,Pr(\gamma-1)M^2}\frac{\partial T}{\partial y}\right)_{C_+}
$$
(6)

Similarly, the fluxes entering the cylinder $B_1A_2B_2\,B_1'A_2'B_2'$ from the wall form the row matrix

$$
g_{w-} = -S\left(0, \frac{-1}{Re}\frac{\partial u}{\partial y}, p - \frac{4}{3Re}\frac{\partial v}{\partial y}, \frac{-1}{Re\,Pr(\gamma-1)M^2}\frac{\partial T}{\partial y}\right)_{C_-}
$$
(7)

where S is the area of the surface $B_1B_2\,B_1'B_2'$ and C_+ and C_- are located immediately above and below the centroid C of the rectangle $B_1B_2\,B_1'B_2'$, respectively. When the mirror image conditions are applied, the total fluxes entering the cylinder $QB_1A_2B_2\,Q'B_1'A_2'B_2'$ from the wall are given by

$$
g_w = g_{w+} + g_{w-} = -2S\left(0, \frac{-1}{Re}\frac{\partial u}{\partial y}, 0, \frac{1}{Re\,Pr(\gamma-1)M^2}\frac{\partial T}{\partial y}\right)_{C_+}
$$
(8)

In the current treatment, the surviving x-momentum flux is treated as a source term in the flux balance in the conservation element. Furthermore, the surviving energy flux represents the heat transfer between the fluid and wall. In other words, if the surviving energy flux is zero, the wall is regarded as an insulated boundary. Essentially, the shear stress exerted on the fluid by the wall is modeled as a source term in one part of the local space–time flux conservation over the basic conservation element (CE$^{(2)}$), as shown in Fig. 1c in the vicinity of the wall boundary. Hence, the current treatment becomes the conventional slip condition for inviscid flows, that is, $1/Re = 0$, because only mirror image conditions are imposed. Consequently, the current boundary treatment is a unified treatment, suitable for both slip and nonslip boundaries.

III. Results and Discussion

Figure 2 is a schematic of the computational domain considered in the present investigation of the vorticity production in two-dimensional shock diffraction around a convex corner. This domain is used as the basis for CE/SE simulations using Euler and laminar Navier–Stokes solvers to analyze 1) the shock wave diffraction itself and 2) the reflected shock/vortex interaction. Figure 2 shows a planar shock wave with a Mach number of M_s propagating downstream along a tube, diffracting around a convex corner with a diffracting angle of θ_d, and then exiting the computational domain (without a horizontal wall) downstream of the convex corner. As already stated,

Table 1   Comparison of rate of circulation production in shock diffraction for various θ_d and M_s

θ_d, deg	M_s							
	1.1	1.2	1.3	1.4	1.5	1.6	1.7	3.0
75								
Sun and Takayama[11]	0.115	0.326	0.606	0.933	1.30	1.67	2.09	8.98
CE/SE	0.110	0.320	0.600	0.928	1.293	1.678	2.079	8.769
90								
Sun and Takayama[11]	0.134	0.364	0.657	0.990	1.36	1.74	2.15	9.16
CE/SE	0.129	0.356	0.648	0.986	1.357	1.745	2.148	9.110
105								
Sun and Takayama[11]	0.145	0.386	0.681	1.019	1.39	1.77	2.175	9.25
CE/SE	0.142	0.381	0.678	1.017	1.386	1.773	2.175	9.294

Fig. 2   Schematic of computational domain.

Fig. 3   Vortical structure in shock diffraction with $M_s = 1.5$ and $\theta_d = 90$ deg: a) experimental photograph[16] and b) numerical solution of Euler solver with coarse grid.
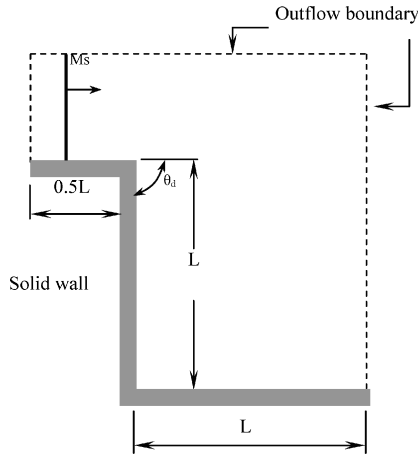
this study also addresses the vorticity production introduced by the reflected shock/vortex interaction. The diffracted shock wave is reflected from the horizontal wall located downstream of the convex corner. The strength of the main vortex is evaluated on the basis of the rate of circulation production. The circulation is related to the vorticity with the following equation:

$$\Gamma = \int_L V \cdot \mathrm{d}l = \int_S \omega \cdot \mathrm{d}s \qquad (9)$$

where the vorticity ω contains component $\partial v/\partial x - \partial u/\partial y$, which can be obtained directly from the CE/SE solution without difficulty. Therefore, in this paper, the numerical calculation of the circulation is directly from summing the vorticity over each individual surface area. The outflow boundaries, indicated by the dashed lines in Fig. 2, are specified as nonreflection boundaries. Finally, slip and nonslip conditions are imposed at the solid walls for inviscid and viscous flows, respectively.

A.   Validation of Euler/Navier–Stokes Solvers

To validate the accuracy of the CE/SE solver, this study compares the CE/SE Euler solutions qualitatively with the experimental results presented by Yang,[18] shown in Fig. 3a, for a shock wave with a Mach number of $M_s = 1.5$ diffracting around a 90-degree convex corner. The study then performs a quantitative evaluation of the rate of circulation production in a shock wave with different Mach numbers diffracting around convex corners with various diffracting angles.

A standard numerical diagnostic feature is to plot the solution contours in density using the postprocessing software, for example, Tecplot. In this paper, the numerical results are presented in density contour by selecting the zebra icon in Tecplot. The numerical interferogram is therefore produced. Figure 3b presents the numerical interferogram obtained from the CE/SE Euler solver for the diffraction of a shock wave around a 90-degree convex corner. It can be seen that the vortical flow structure comprises a main vortex and a contact surface, but has no secondary vortex below the slipstream
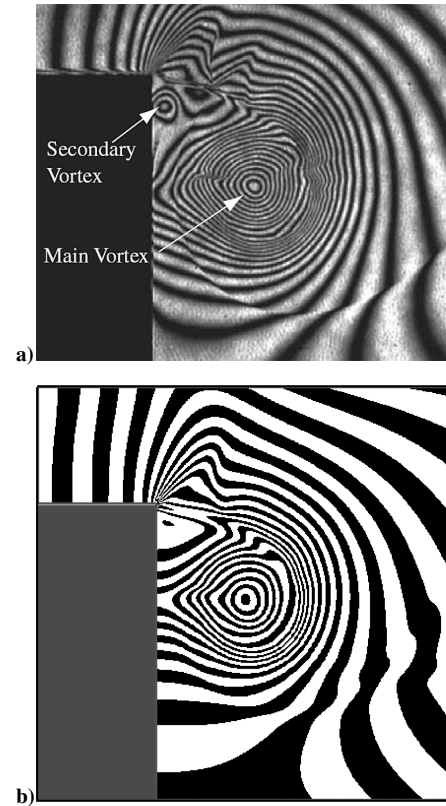
nor between the corner and the main vortex. It is known that the secondary vortex is caused by the separation of the boundary layer on the downstream wall. However, because the Euler simulation considers neither the viscous effects nor the heat conduction effects, the secondary vortex is not apparent in this solution. Table 1 summarizes the rates of circulation production predicted by the CE/SE Euler solver for shock waves with different Mach numbers diffracting around various convex corners. Note that the data in Table 1 are normalized by RT_0, where R is the gas constant and T_0 is the temperature in front of the incident shock wave. In general, the circulation calculation is performed only in the perturbed region behind the diffracted shock. However, in this study the circulations are calculated over the complete computational domain because the unperturbed region provides no contribution to the circulation effect. It can be seen that the rate of circulation production increases as the Mach number and diffracting angle increase. In other words, the strength of the main vortex increases at higher values of Mach number and diffracting angle. From the results already presented, it is clear that the current CE/SE Euler solutions are in good qualitative agreement with Yang's[18] experimental result and in good quantitative agreement with the circulation production results reported by Sun and Takayama.[11]
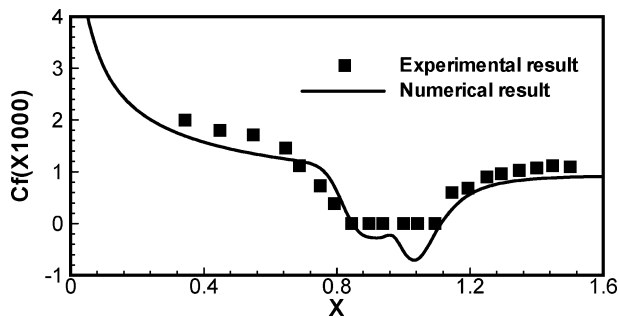
Fig. 4 Skin-friction distribution along solid wall in shock/boundary-layer interaction problem with Re = 2.69E5.

The problem of shock wave/boundary-layer interaction is often used as a standard test for the Navier–Stokes solver. In this study the case is considered of an incoming shock wave with a Mach number of 2.0 and emanating from the upper-left-hand corner of the computational domain when it impinges on the solid wall at an angle of 32.6 deg with respect to the wall. The inlet boundary condition employs the specified inlet boundary condition, and the flow on the top boundary is specified to form an oblique shock, which is calculated based on the oblique shock condition to form the desired shock wave angle. Because the first tripartition of the bottom boundary and right boundary is the outlet boundary, a nonreflection boundary condition is used. Furthermore, nonslip conditions are imposed on the solid wall on the remainder of the bottom wall. Because the impinging shock is strong, boundary-layer separation occurs at the impinging point on the wall, and the resulting flow pattern is highly complicated. To resolve the boundary layer, the grid points are clustered to the solid wall. The first grid point to the solid wall is 5×10^{-5} of the domain height. There are 240,000 grid points covering the whole computational domain. Figure 4 shows a comparison of the results for the skin-friction distribution along the solid wall obtained experimentally by Hakkinen et al.[19] (square symbols) with those obtained from the present CE/SE Navier–Stokes solver (solid line) for the case of $Re = 2.96 \times 10^5$. As in the case of the CE/SE Euler solver discussed earlier, it can be seen that the results of the Navier–Stokes solver are in good agreement with those obtained experimentally.

B. Small Vortices Along Slipstream

According to the numerical results of Sun and Takayama,[11] small vortices may appear in the slipstream behind the diffracted shock wave. However, although the main vortical structures predicted numerically are in good agreement with the experimental results, these small vortices have never been observed experimentally. Nevertheless, other researchers have identified the same phenomena in their simulations of shock wave diffraction around a convex corner and Mach reflection over a wedge using a variety of different numerical schemes. Because the shear layer is unstable and Kelvin–Helmholtz instability develops and eventually evolves into small vortices, Sun and Takayama[11] pointed out that the rollup phenomenon observed in numerical simulation remains a controversial issue.

To investigate the rollup phenomenon further, in this study various grid sizes are employed to simulate the shock wave diffraction of an incident planar shock wave of Mach number $M_s = 1.5$ around a 90-deg convex corner. The adopted computational domain without a horizontal wall located downstream of the convex corner is shown in Fig. 2. Figures 3b and 5a present the CE/SE Euler solutions obtained using a coarse grid (54,000 cells) and a fine grid (486,000 cells), respectively. In both cases, the slipstream initiation and main vortex are clearly visible. However, the presence of small vortices along the slipstream is not evident in either Fig. 3b or 5a. The small vortices reported by Sun and Takayama[11] were identified using a fine-grid Euler solver and the laminar Navier–Stokes solver, but were not visible in the turbulence solution provided by k–ε turbulence modeling. To establish whether or not the CE/SE method identifies these small vortices, the simulation described earlier was repeated using the Euler solver with a finest grid (1,944,000 cells) and the laminar Navier–Stokes solver, respectively. The corre-
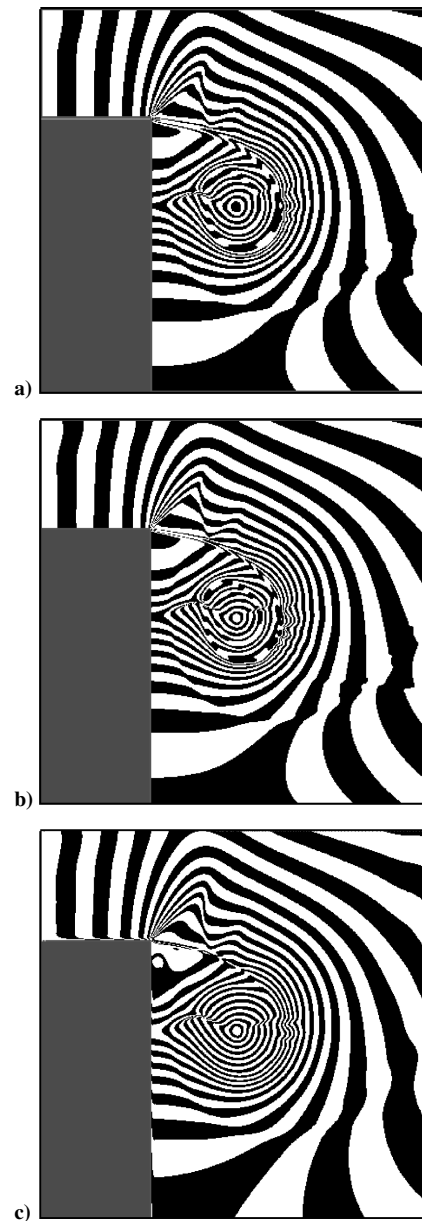

Fig. 5 Numerical results for vortical structure in shock wave diffraction: a) fine grid Euler solution, b) very fine grid Euler solution, and c) laminar Navier–Stokes solution.

sponding results are presented in Figs. 5b and 5c, respectively. In this simulation, the Navier–Stokes solver with a finer nonuniform grid (791,280 cells) in the 120×120 mm domain, had a minimum grid size of 30 μm, and considered the Reynolds number to be approximately 4.118425×10^6 to establish a representative shock velocity. The results in Fig. 5c confirm that the CE/SE Navier–Stokes solver successfully captures all of the features of the shock diffraction, including the boundary layer on the solid wall and the secondary vortex near the corner. However, the small vortices are not evident along slipstream, even in the long time marching. The results presented confirm that the solutions of the CE/SE method are in good agreement with the experimental results when the Navier–Stokes or Euler solvers are applied, regardless of the grid size specified in the latter. Moreover, the CE/SE method successfully suppresses the small vortices, while preserving the essential features of the vortical structure.

C. Vorticity Production in Shock Wave Diffraction

When the computational domain, shown in Fig. 2, without a bottom wall behind the backward step was used, the vorticity production associated with shock wave diffraction was investigated by considering the rate of circulation production. To verify that the numerical
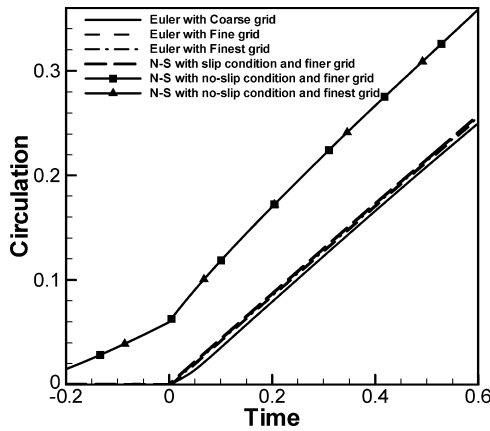
Fig. 6 Convergence of circulation time history for different grid systems.

results are independent of the grid system, Fig. 6 shows the circulation production for the diffraction of a shock wave with an incident Mach number of $M_s = 1.5$ around a 90-deg convex corner using different mesh systems, that is, the coarse grid, fine grid, and finest grid, indicated by the solid line, dashed line, and dashed–dot line, respectively. The time is set to zero at the point when the incident shock wave arrives at the corner. Hence, the Euler solutions assume that no circulation production takes place before this event. Figure 6 confirms that the present simulation results are nearly independent of the grid system employed in the solver. In a more realistic simulation, the Navier–Stokes equations were solved to consider the effects of viscosity and heat conductivity on the production of circulations in the perturbed region. The bold dashed line in Fig. 6 indicates the circulation production predicted by the Navier–Stokes solver when a slip condition is imposed on the solid wall. It is observed that the absence of a boundary layer prevents the production of circulations before the shock wave diffraction. The circulation production results in Fig. 6 demonstrate the role played by viscous effects and heat conductivity in forming the shock diffraction structure. Even through the viscous effects and heat conductivity are considered, only a slight difference is evident between the Euler solution and the Navier–Stokes solution for the case in which no boundary layer exists. When the finer and finest grid system were utilized, the simulation was repeated using the Navier–Stokes solver and imposing no-slip conditions on the solid wall. In this case, vorticity production occurs before the diffraction of the incident shock wave as a result of the boundary layer developed behind the incident shock on the solid wall, and the Navier–Stokes results are nearly independent of the grid system employed in the solver.

Figures 7a and 7b present the circulation production for shock waves diffraction with various incident Mach numbers around a 75-deg convex corner and around corners of various diffracting angles at a constant incident Mach number of 1.5, respectively. It can be seen that the rate of circulation production increases as the incident Mach number and the diffracting angle increase, but it hardly change when the incident Mach number is greater than 3.0 and the diffracting angle greater than 105 deg. Figure 7c shows a comparison of the circulation production results predicted by the Euler solver (dashed line) with those obtained from the Navier–Stokes solver (solid line) for the case of incident shocks with Mach numbers of $M_s = 1.5$ and 2.5 diffracting around a 90-deg convex corner. In the Navier–Stokes solutions, the rate of circulation production increases linearly as a result of the boundary layer that developed before the arrival of the incident shock wave at the corner. The boundary layer that developed at the solid wall and the secondary vortex originating at the diffraction corner cause the circulation production predicted by the Navier–Stokes solver to be greater than that obtained using the Euler solver.

D. Reflected Shock/Vortex Interaction

The Euler and Navier–Stokes solvers were employed to investigate the interaction between the reflected shock wave from the
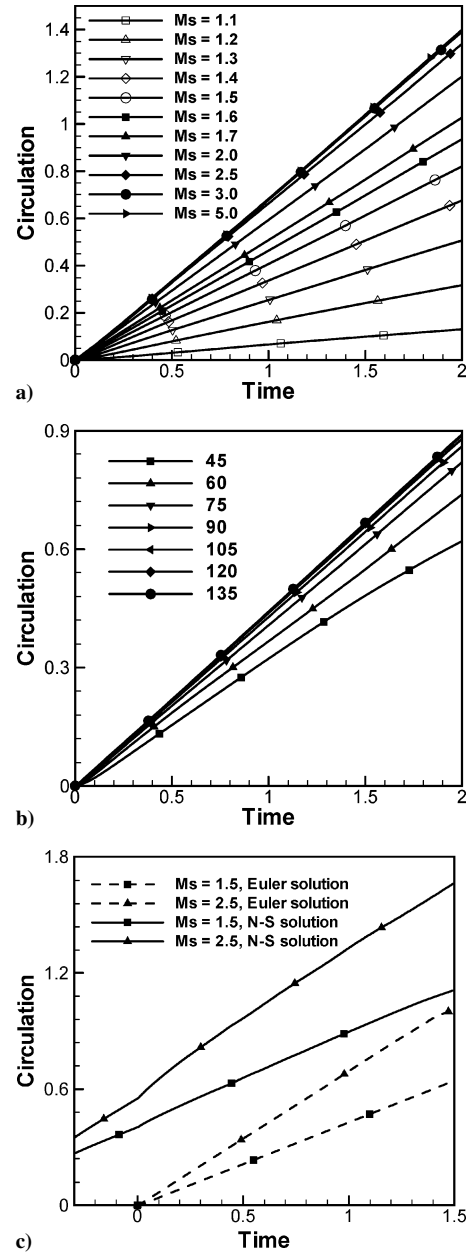

Fig. 7 Time history of circulation: a) effect of incident Mach number at constant $\theta_d = 75$ deg, b) effect of diffracting angle at constant $M_s = 1.5$, and c) comparison of circulation production in Euler and Navier–Stokes solutions with $M_s = 1.5$ and 2.5.

bottom wall and the main vortex. The simulations utilized the computational domain shown in Fig. 2 with a backward step of height $L/2$.

Figure 8 shows the evolution of an incident shock wave with a Mach number of 2.5 as it diffracts around a 75-deg convex corner. The shock diffraction induces a terminator, a slipstream, a secondary shock, a contact surface, a main vortex, and a vortex shock. Observe that the interaction of the secondary shock (bounded by the terminator and the slipstream) with the main vortex causes the main vortex to lose its circular shape. The incident shock wave propagates farther downstream and impinges on the bottom wall to form a regular reflection. The reflected shock wave subsequently interacts with the contact surface, the main vortex, and the slipstream, as shown in Figs. 8a and 8b. Figure 8b indicates that the reflected shock wave is deformed and that the secondary shock divides the reflected shock into two parts, namely, one part behind the secondary shock and a second part in front of the secondary shock. The main vortex structure is deformed as a result of its interaction with the first part of the reflected shock and is constrained by the bottom wall. Once the
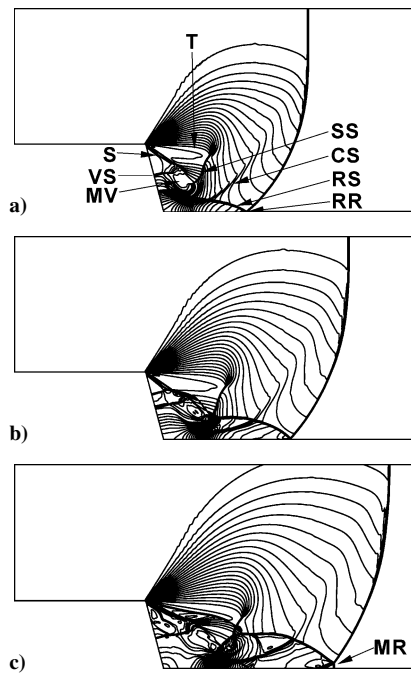
Fig. 8 Numerical results for density distribution of reflected shock/vortex interaction problem for $M_s = 1.5$ and $\theta_d = 75$ deg in Euler simulation; flow structure includes terminator (T), slipstream (S), secondary shock (SS), contact surface (CS), main vortex (MV), vortex shock (VS), reflected shock (RS), regular reflection (RR), and Mach reflection (MR): a) $T^* = 1.2$, b) $T^* = 1.5$, and c) $T^* = 1.8$.
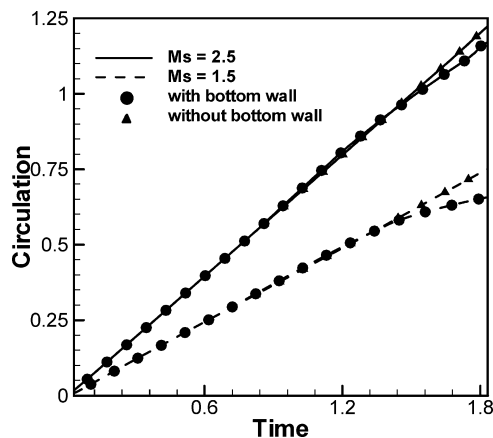

Fig. 9   Effect of bottom wall assumption on circulation production.

reflected shock has passed through the main vortex, it interacts with the slipstream. Meanwhile, the second part of the reflected shock interacts with the contact surface and prompts the formation of a second Mach reflection with the secondary shock. Finally, a delta shock is formed under the terminator by the interaction between the reflected shock wave and the secondary shock wave, as shown in Fig. 8c. The impinging of the reflected wave of the second Mach reflection on the bottom wall results in a further reflection.

Figure 9 shows the circulation production history for incident shock waves with Mach numbers of 1.5 and 2.5, respectively, with and without a bottom wall in the computational domain. The rate of circulation production is no longer constant when the diffracted shock wave is reflected. The reflected shock wave initially interacts with the contact surface and forms a lambda shock at $T^* = 1.2$. As the diffracted shock continues to propagate downstream, the rate of circulation production decreases as the shock reflection configuration transits from a regular reflection to a Mach reflection, and the reflected shock wave interacts with the contact surface, the main vortex, the vortex shock, the slipstream, and the secondary shock.

The flow structure associated with the reflected shock/vortex interaction is complicated. The intensity and shape of the main vortex is changed both by the reflected shock wave and the constraint imposed by the bottom wall. In addition to the reflected shock/vortex interaction, an interaction occurs between the reflected shock wave and the contact surface, slipstream, secondary shock, and bottom wall. However, the interaction with the secondary vortex cannot be observed in the Euler simulation. To perform a more realistic simulation, the viscous effect and heat conductivity was taken into consideration and the Navier–Stokes solver was used to investigate the case of the diffraction of an incident shock wave with a Mach number of 2.5 around a 90-deg convex corner. A nonslip condition was imposed on the solid wall surface and the wall was assumed to be isothermal. The density distributions obtained by solving the laminar Navier–Stokes and Euler equations under these conditions are shown in Figs. 10a and 10b, respectively. In the Navier–Stokes solution, a boundary layer develops on the solid walls before the shock wave diffraction. This effect is not noted in the Euler solution. As a consequence, the flow features in the Navier–Stokes solution are self-similar, apart from when they are influenced by the boundary layer. In the Euler solution, the reflection of the diffracted shock wave from the bottom wall, and the subsequent interaction of the reflected shock wave with the original diffracted structure, particularly the secondary vortex interaction, is not observed.

Figure 10c shows a comparison of the vorticity production results for incident shock waves with Mach numbers of 1.5 and 2.5,
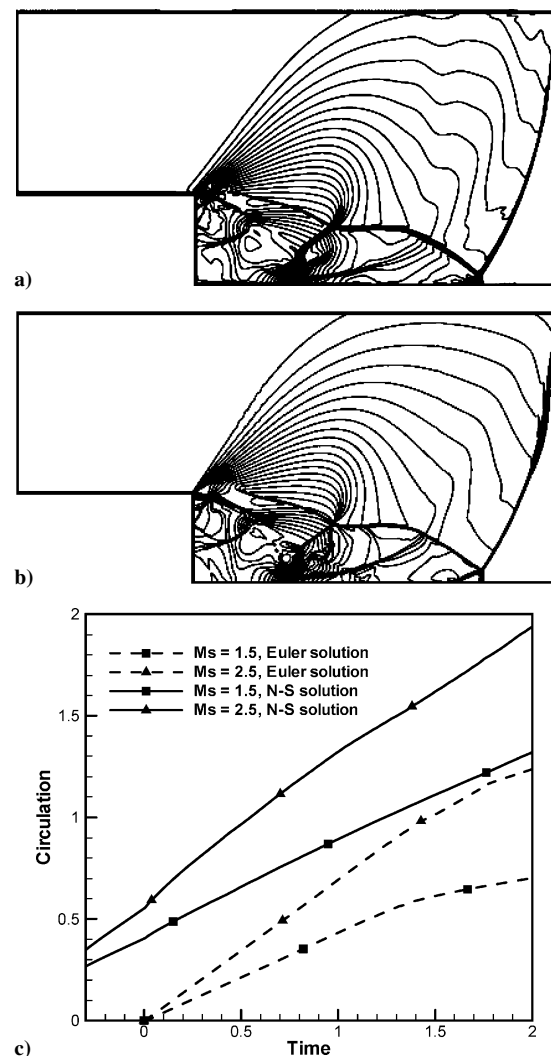

Fig. 10   Numerical results for density distribution of reflected shock/vortex interaction problem for $M_s = 1.5$ and $\theta_d = 90$ deg: a) laminar Navier–Stokes solution, b) Euler solution, c) comparison of circulation production results obtained using Euler and Navier–Stokes solvers.

respectively, obtained using the laminar Navier–Stokes and Euler solvers. Because a high-velocity gradient is established on the upstream solid wall of the backward step, significant vorticity is generated in the boundary layer before the incident shock wave arrives at the corner. Even though the flow moves upward on the horizontal wall close to the corner and the secondary vortex lying between the main vortex and the corner generates a positive (counterclockwise) vorticity, the overall vorticity remains negative (clockwise) because it is dominated by the slipstream, the main vortex, and the boundary layer, which flows downward. It can be seen that the shock wave reflection on the bottom wall and the shock/vortex interaction cause the rate of circulation production to become nonconstant in the Euler simulations. In the Navier–Stokes solutions, the rate of circulation production fails to converge to a constant as a result of boundary-layer effects.

IV.   Conclusions

The characteristics of shock wave diffraction around a convex corner using the space–time CE/SE method and Euler and laminar Navier–Stokes solvers have been investigated. Different grid systems have been implemented in the Euler simulation to investigate the grid size effect on the observation of small vortex instabilities along the slipstream. Although reported in the numerical results of Sun and Takayama obtained using adaptive grids, the rollup of small vortices along the slipstream has not been observed in the present CE/SE Euler and Navier–Stokes simulations. The present results obtained by the CE/SE Navier–Stokes solver taking the viscous effects and heat conductivity into account are consistent with the experimental findings presented previously for the boundary layer and the secondary vortex.

The vorticity production formed during shock wave diffraction and the subsequent interaction between the reflected shock wave and the main vortex have been investigated numerically using the Euler and laminar Navier–Stokes solvers, respectively. The results have shown that the shock wave diffraction structure obtained without the bottom wall is self-similar in the Euler simulation and is self-similar in the laminar Navier–Stokes simulation other than when influenced by the boundary layer on the solid wall. Furthermore, it has been shown that, when the diffracted shock impinges the bottom wall, a shock wave reflection configuration is established. This configuration transits from a regular reflection to a Mach reflection as the shock wave continues to diffract downstream. In addition to the reflected shock/vortex interaction, the reflected shock and the secondary shock cause a second shock wave reflection during diffraction of a strong shock wave. This reflection also influences the rate of vorticity production. Finally, the numerical results have indicated that, both in Euler and Navier–Stokes simulations, the rate of vorticity production increases as the incident shock strength and diffracting angle increase, but remains virtually constant when the diffracting angle exceeds 90 degrees.

Acknowledgments

References

[1]Howard, L., and Mathews, D., "On the Vortices Produced in Shock Diffraction," *Journal of Applied Physics*, Vol. 27, No. 3, 1956, pp. 223–231.

[2]Skews, B., "The Shape of a Diffracting Shock Wave," *Journal of Fluid Mechanics*, Vol. 29, Pt. 2, 1967, pp. 297–304.

[3]Skews, B., "The Perturbed Region Behind a Diffraction Shock Wave," *Journal of Fluid Mechanics*, Vol. 29, Pt. 4, 1967, pp. 705–720.

[4]Dosanjh, D., and Weeks, T., "Interaction of a Starting Vortex as well as a Vortex Street with a Traveling Shock Wave," *AIAA Journal*, Vol. 3, No. 2, 1965, pp. 216–223.

[5]Schardin, H., "Measurement of Spherical Shock Waves," *Communications of Pure and Applied Mathematic*, Vol. 7, No. 1, 1954, pp. 223–243.

[6]Evans, R., and Bloor, M., "The Starting Mechanism of Wave-Induced Flow Through a Sharp-Edged Orifice," *Journal of Fluid Mechanics*, Vol. 82, Pt. 1, 1977, pp. 115–128.

[7]Bazhennova, T., Gvozdeva, L., and Nettleton, M., "Unsteady Interactions of Shock Wave," *Progress in Aerospace Science*, Vol. 21, No. 1, 1984, pp. 249–331.

[8]Takayama, K., and Inoue, O., "Shock Wave Diffraction over a 90 Degree Sharp Corner," *Shock Waves*, Vol. 1, No. 4, 1991, pp. 301–312.

[9]Hillier, R., "Computation of Shock Wave Diffraction at a Ninety Degrees Convex Edge," *Shock Waves*, Vol. 1, No. 2, 1991, pp. 89–98.

[10]Sun, M., and Takayama, K., "The Formation of a Secondary Shock Wave Behind a Shock Wave Diffracting at a Convex Corner," *Shock Waves*, Vol. 7, No. 5, 1997, pp. 287–295.

[11]Sun, M., and Takayama, K., "A Note on Numerical Simulation of Vortical Structures in Shock Diffraction," *Shock Waves*, Vol. 13, No. 1, 2003, pp. 25–32.

[12]Kleine, H., Ritzerfeld, E., and Grönig, H., "Shock Wave Diffraction at a Ninety Degree Corner," *Computational Fluid Dynamics Journal*, Vol. 12, No. 2, 2003, pp. 142–158.

[13]Sun, M., and Takayama. K., "Vorticity Production in Shock Diffraction," *Journal of Fluid Mechanics*, Vol. 478, 2003, pp. 237–256.

[14]Chang, S., "The Method of Space-Time Conservation Element and Solution Element—A New Approach for Solving the Navier–Stokes and Euler Equations," *Journal of Computational Physics*, Vol. 119, No. 2, 1995, pp. 295–324.

[15]Chang, S., Wang, X., and Chow, C., "The Space–Time Conservation Element and Solution Element Method: A New High-Resolution and Genuinely Multidimensional Paradigm for Solving Conservation Laws," *Journal of Computational Physics*, Vol. 156, No. 1, 1999, pp. 89–136.

[16]Zhang, Z., Yu, S., Wang, X., Chang, S., Himansu, A., and Jorgenson, P., "The CE/SE Method for Navier–Stokes Equations Using Unstructured Meshes for Flow at All Speeds," AIAA Paper 2000-0393, Jan. 2000.

[17]Zhang, Z., Yu, S., and Chang, S., "A Space-Time Conservation Element and Solution Element Method for Solving the Two- and Three-Dimensional Unsteady Euler Equations Using Quadrilateral and Hexahedral Meshes," *Journal of Computational Physics*, Vol. 175, No. 1, 2002, pp. 168–199.

[18]Yang, J., "Experimental and Theoretical Study of Weak Shock Wave," Ph.D. Dissertation, Inst. of Fluid Science, Tohoku Univ., Sendai, Japan, 1995 (in Japanese).

[19]Hakkinen, R., Greber, I., and Trilling, L., "The Interaction of an Oblique Shock Wave with a Laminar Boundary Layer," NASA Memo 2-18-59W, March 1959.

S. Aggarwal
Associate Editor